30 October 2025

Understanding Interface-Driven Dynamics of Microbial Carbonate Precipitation through DNA-Driven Tethering

Yoo Kyung Go[1], Tali Dotan[1], Chao-Chi Kuo[1], Melanie Gut[1], Ariel Furst[1]

1. Massachusetts Institute of Technology

Abstract

The energy- and carbon-intensity of cement production and maintenance is prohibitive for the growing global demand. A key sustainable alternative is microbially-induced carbonate precipitation (MICP), a biological process performed by many diverse microbes, most often at abiotic interfaces. Most studies of MICP have relied on bulk solution conditions, which fail to replicate the native environment of these microbes. By tethering microbes to abiotic substrates using DNA as “Velcro,” MICP at an abiotic interface can be effectively studied and controlled. The precipitate generated at these interfaces shows key morphological and kinetic differences from that generated in bulk solution. These differences highlight the critical need for approaches to enable the study of sustainable processes in relevant conditions. Our DNA “Velcro” approach serves as a universal method to generate microbial monolayers at abiotic interfaces, enabling the study of their behavior under relevant conditions. These learnings further support technology scaling, enabling decarbonization of sectors associated with extremely high emissions.

Keywords

Microbially-Induced Carbonate Precipitation, Interfacial Engineering, DNA Velcro

Posted on 30 October 2025 — CC-BY-NC-ND 4.0 — This is a preprint and has not been peer reviewed. Data may be preliminary. —
https://doi.org/10.26434/chemrxiv-2025-6pdcx

Understanding Interface-Driven Dynamics of Microbial Carbonate Precipitation through DNA-Driven Tethering

*Yoo Kyung Go,[1] Tali Dotan,[1] Chao-Chi Kuo,[1] Melanie Gut,[1] Ariel L. Furst[1]**

[1]Department of Chemical Engineering, Massachusetts Institute of Technology; Cambridge, MA, 02139, United States of America.

ABSTRACT

The energy- and carbon-intensity of cement production and maintenance is prohibitive for the growing global demand. A key sustainable alternative is microbially-induced carbonate precipitation (MICP), a biological process performed by many diverse microbes, most often at abiotic interfaces. Most studies of MICP have relied on bulk solution conditions, which fail to replicate the native environment of these microbes. By tethering microbes to abiotic substrates using DNA as "Velcro," MICP at an abiotic interface can be effectively studied and controlled. The precipitate generated at these interfaces shows key morphological and kinetic differences from that generated in bulk solution. These differences highlight the critical need for approaches to enable the study of sustainable processes in relevant conditions. Our DNA "Velcro" approach serves as a universal method to generate microbial monolayers at abiotic interfaces, enabling the

https://doi.org/10.26434/chemrxiv-2025-6pdcx **ORCID:** https://orcid.org/0000-0001-9583-9703 Content not peer-reviewed by ChemRxiv. **License:** CC BY-NC-ND 4.0

study of their behavior under relevant conditions. These learnings further support technology scaling, enabling decarbonization of sectors associated with extremely high emissions.

INTRODUCTION

Construction to enhance global infrastructure is expected to cost between 60 and 95 trillion dollars in the next 25 years, driven by the growing population.[1] With construction comes increased demand for concrete, which is currently the highest-consumed product besides water globally. In fact, China used as much concrete between 2011 and 2013 as the US did during the 20th century.[2–4] Concrete is comprised of cement and filler, with cement serving as a critical binding agent that imbues concrete with its useful properties. Yet, these benefits are accompanied by significant carbon emissions; concrete manufacture is responsible for 8% of global emissions,[5] nearly 2.5 billion metric tons of CO_2 equivalents in 2023.[6] To achieve global sustainability goals, the cement industry must be decarbonized.

Efforts to curb cement-associated emissions range from decarbonizing production to minimizing use in new construction. An emerging approach involves the use of biological processes to generate cement without the associated emissions. Many native microbial species naturally produce the basis of cement (calcium carbonate), through a biomineralization process termed microbially-induced carbonate precipitation (MICP).[7–10] In fact, this process has been applied well beyond the generation of construction materials, with uses ranging from enhanced soil weathering to prevention of shoreline erosion.[7,11–14]

Because of its ubiquity, many diverse microbes can perform MICP via several different mechanisms, including ureolysis[15,16] and sulphate reduction.[17,18] Ureolysis is especially prevalent in large-scale MICP applications due to the ability to control the rate of this process through addition of exogeneous urea. However, as with cement, urea production is associated with

https://doi.org/10.26434/chemrxiv-2025-6pdcx **ORCID:** https://orcid.org/0000-0001-9583-9703 Content not peer-reviewed by ChemRxiv. **License:** CC BY-NC-ND 4.0

significant emissions, as ammonia used in its generation is currently produced by the energy-intensive Haber-Bosch process, representing as much as 2% of global emissions.[19]

Some microbes perform MICP autotrophically,[20,21] though they are less well-characterized and therefore less frequently used in biotechnology despite their promise to decrease emissions associated with MICP. To enable autotrophic MICP in large-scale applications, this process and its products must be characterized. A critical challenge with MICP studies is their reliance on bulk characterization of calcium carbonate produced by microbes. Nonetheless, the majority of MICP occurs at solid-liquid or solid-gas interfaces.[22,23] Thus, to study autotrophic MICP at interfaces, control over the two-dimensional spatial organization of the microbes involved in these processes is needed.

Here, we report the characterization of MICP from the mixotrophic *Rhodospirillium rubrum* (*R. rubrum*) immobilized on a glass substrate and sitting at a glass-liquid interface. We employ a simple, bio-compatible approach to generate a single layer of cells on the glass through the use of DNA "Velcro".[24–29] This approach, also termed DNA-based cell adhesion, involves one surface modified with short, synthetic DNA strands and microbes chemically modified with the complementary strand. DNA hybridization supports microbial adhesion to the surface. Once immobilized, microbes perform MICP in a monolayer, allowing us to monitor carbonate precipitation rate and particle crystallinity at the interface. Through characterization of the differences between microbes immobilized at an abiotic substrate and those in bulk solution, we establish the role of the interface in the microbial behavior. By developing DNA "Velcro" for microbial monolayer generation, we have a universal approach to study the behavior of microbes at abiotic surfaces and support their ability to produce materials under environmentally-relevant conditions.

https://doi.org/10.26434/chemrxiv-2025-6pdcx **ORCID:** https://orcid.org/0000-0001-9583-9703 Content not peer-reviewed by ChemRxiv. **License:** CC BY-NC-ND 4.0

RESULTS

R. rubrum-based MICP in bulk solution

A variety of environmentally-derived microbes are capable of MICP, and here we study the native soil microbe *R. rubrum* as a model system. *R. rubrum* are Gram-negative, purple non-sulfur photosynthetic bacteria with a size of 0.8 – 1 μm (Figure 1A).[30–32] This strain can grow under photoautotrophic, photoheterotrophic, or chemoheterotrophic conditions, and it can metabolize acetate to produce bicarbonate heterotrophically due to its carbonic anhydrase (Figure 1B).[31–35] In the presence of high concentrations of calcium ions, *R. rubrum* activity results in the precipitation of calcium carbonate particles (Figure 1C).

When grown heterotrophically on acetate in bulk solution, calcium carbonate particles with defined crystallinity form in solution. Crystalline particles were analyzed by XRD, confirming the generation of this calcium carbonate from among the calcium carbonate polymorphs (calcite, vaterite, and aragonite).[36,37] XRD analysis confirmed that these particles are calcite, the most stable form of calcium carbonate (Figure 1D). This behavior in *R. rubrum* is well-established in defined, laboratory settings. Yet in native niches, this microbe mainly performs MICP at abiotic interfaces such as soil granules. Understanding the interfacial behavior of this microbe at relevant interfaces such as silicates is less well studied but is nevertheless critical to characterize the MICP process. Therefore, we sought to characterize the behavior of this species when it is immobilized at a relevant interface.

https://doi.org/10.26434/chemrxiv-2025-6pdcx **ORCID:** https://orcid.org/0000-0001-9583-9703 Content not peer-reviewed by ChemRxiv. **License:** CC BY-NC-ND 4.0

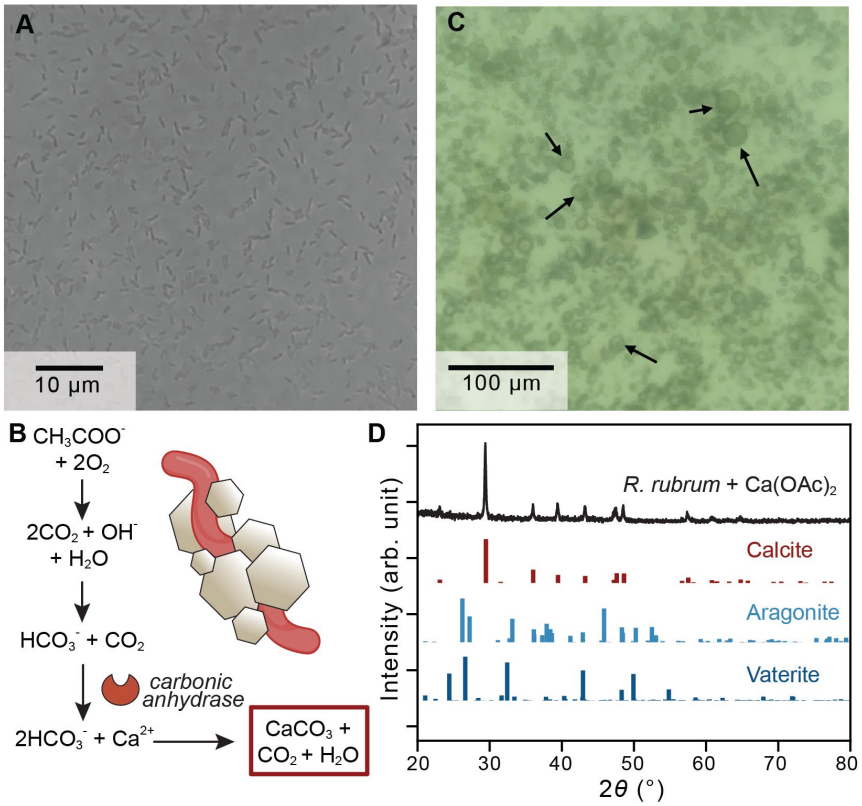


Figure 1. Microbial-induced carbonate precipitation (MICP) of *R. rubrum* in bulk solution. *R. rubrum* produces calcium carbonate particles from calcium ions: (A) Optical microscopy image of *R. rubrum* in nutrient broth media (in grey scale). (B) Graphical illustration of heterotrophic metabolism of acetate by *R. rubrum* to generate bicarbonate ions which further precipitates as calcium carbonate in presence of calcium ions. (C) Optical microscopy image of *R. rubrum* and calcium carbonate particles (marked by arrows). The cells were cultured in nutrient broth to reach OD_{600} of 1, followed by adding 1 equivalent volume of 0.1 M calcium acetate solution. The image was taken after incubation for 40 hours at 30°C. (D) Powder XRD pattern of calcium carbonate particles synthesized by *R. rubrum*. The calcium carbonate particles were collected for characterization after a week of reaction at 30°C. The vertical line plots at the *bottom* show reference diffraction of calcite,[38] aragonite,[39] and vaterite[40] from *top* to *bottom*. Bragg peaks were generated using the cif files using software VESTA.[41]

https://doi.org/10.26434/chemrxiv-2025-6pdcx **ORCID:** https://orcid.org/0000-0001-9583-9703 Content not peer-reviewed by ChemRxiv. **License:** CC BY-NC-ND 4.0

Chemistry of DNA "Velcro"-based cell immobilization

To control the immobilization of *R. rubrum* and locally produce calcium carbonate on a 2D solid support, we employed DNA hybridization-based cell adhesion (DNA "Velcro"). DNA "Velcro" is an established, non-genetic approach to support the immobilization of nearly any cell (prokaryotic or eukaryotic) on a substrate.[24–29] Generally, this approach involves substrate modification with short, synthetic single-stranded DNA and chemical attachment of the complementary sequence to the surface of microbes. When the cell is sufficiently close to the modified substrate, DNA hybridization supports the capture of these cells on the substrate, enabling precise placement of microbes through control over DNA placement on a substrate.[27,28]

Glass substrates are readily modified with DNA through a well-established process involving silanization to display a chemical handle for subsequent biomolecule modification. Here, we employed APTES ((3-aminopropyl)triethoxysilane) to allow for amide bond formation at the substrate surface to display an *o*-nitrophenol. This moiety can then be chemically reduced to an *o*-aminophenol, which readily reacts with aniline-modified DNA via bio-orthogonal oxidative coupling to install DNA on the glass (*bottom*, Figure 2A).[29]

Similarly, robust modification of microbes with single-stranded DNA is accomplished through a two-step approach involving the initial generation of aldehydes on the surface of microbes through the oxidation of peptidoglycan sugars. These aldehydes react with hydrazine-modified DNA to generate a hydrazide[28] (*top left*, Figure 2A). By drop-casting DNA-modified cells onto glass functionalized with the complementary DNA, cells are tethered to the substrate surface through DNA hybridization (Figure 2B). Upon addition of a calcium-rich solution to the immobilized cells, MICP is observed (*top right*, Figure 2A).

https://doi.org/10.26434/chemrxiv-2025-6pdcx **ORCID:** https://orcid.org/0000-0001-9583-9703 Content not peer-reviewed by ChemRxiv. **License:** CC BY-NC-ND 4.0

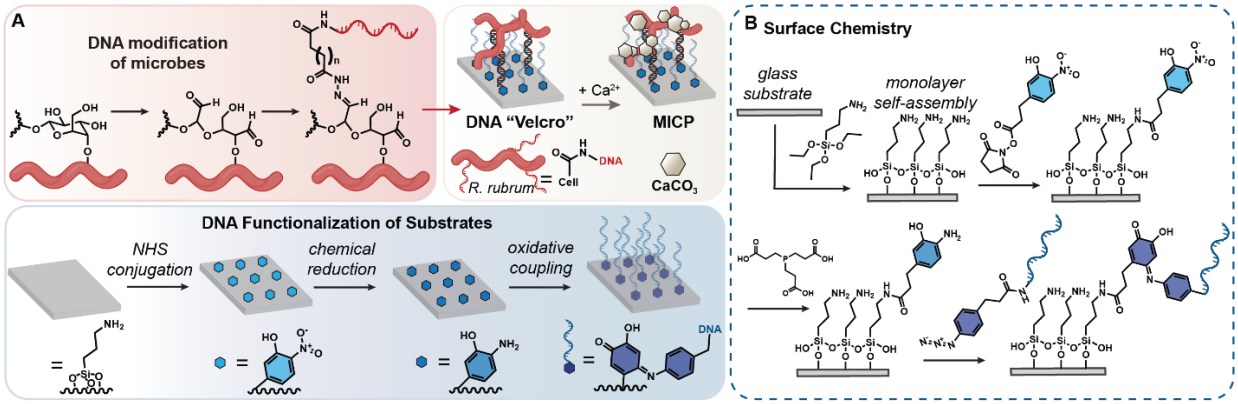


Figure 2. Overview of calcium carbonate production via DNA-assisted microbes on surfaces. (A) Direct localization of microbes on surfaces by DNA-Velcro followed by microbial-induced carbonate precipitation (MICP). (*Top*) direct DNA conjugation on cells, (*bottom*) graphical illustration of DNA functionalization of substrates including NHS conjugation, chemical reduction, and oxidative coupling reactions. (B) Overall surface chemistry is shown with the functionalization agent molecules. (3-Aminopropyl)triethoxysilane (APTES) forms self-assembled monolayer (SAM), which is reacted with 2,5-dioxopyrrolidin-1-yl 3-(4-hydroxy-3-nitrophenyl)propanoate for NHS conjugation. Then, the nitrophenyl group was reduced by tris(2-carboxyethyl)phosphine (TCEP), resulting in the formation of 3-(4-hydroxy-3-aminophenyl) group at the terminus of the SAM. This 4-hydroxy-3-aminophenyl group undergoes oxidative coupling with aniline-terminus DNA strand.[29]

https://doi.org/10.26434/chemrxiv-2025-6pdcx **ORCID:** https://orcid.org/0000-0001-9583-9703 Content not peer-reviewed by ChemRxiv. **License:** CC BY-NC-ND 4.0

Analysis of immobilized *R. rubrum* on glass supports

Prior to the investigation of interfacial MICP, we first determined the coverage of tethered *R. rubrum* cells immobilized through DNA "Velcro" (Figure 3A). The cells can be observed following immobilization through staining with Nile blue. This immobilization strategy yields uniform coverage across centimeter-scale substrates (blue, Figure 3B). The uniformity of the cell distribution indicates the successful immobilization of cells due to DNA hybridization. Controls include DNA-modified substrates with unmodified cells and unmodified substrates with DNA-modified cells. For both of these controls, very few cells adhere to the substrate when either the cells or substrate is unmodified. Cell coverage was found to be 1.29 ± 0.63 ($n = 7$) and 0.19 ± 0.09 ($n = 11$) for the number of cells/100 μm^2 (Figure S1).

In addition to our ability to control the overall distribution of cells across a surface, we confirmed the specificity of DNA-directed immobilization. PDMS microwells were generated from a mold (Figure 3D-F) to create a well on the glass substrate. As the DNA-modified cells were only exposed to the area inside the PDMS, we only expect to see cells adhered to the substrate within the well. As is apparent in Figure 3, the cells only adhered to the exposed area. Cell coverage was additionally calculated by ImageJ (Figure S2)[42] from two different samples (Figure S3). Based on this quantification, we determined that an average of 17.3 and 0.6 cells/100 μm^2 inside and outside of the PDMS wells were present, respectively ($n = 3$ and 1, Figure 3C and Table S1). The coverage outside of the PDMS represents two orders of magnitude fewer cells adhered through non-specific immobilization than those adhered through DNA hybridization. Additionally, we do not observe inconsistent distribution of cells within the PDMS wells, as can occur due to attraction between cells and the PDMS. Together, these results demonstrate the power of DNA "Velcro" to controllably generate homogeneous layers of cells within areas defined by simple PDMS molds.

https://doi.org/10.26434/chemrxiv-2025-6pdcx **ORCID:** https://orcid.org/0000-0001-9583-9703 Content not peer-reviewed by ChemRxiv. **License:** CC BY-NC-ND 4.0

This PDMS molding approach circumvents many complications associated with work to chemically pattern the DNA displayed on the glass substrate, which adds complex chemical reactions and requires additional photopatterning steps to accomplish.

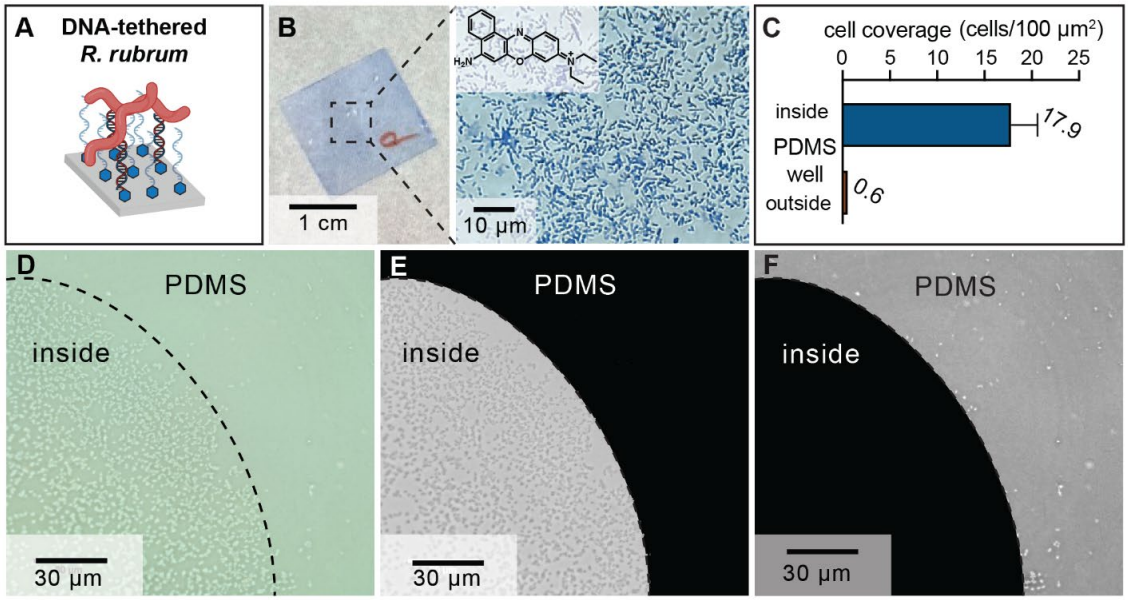


Figure 3. DNA-tethered *R. rubrum* cells on glass substrates. (A) Graphical illustration of DNA-tethered *R. rubrum* cells on glass substrates. (B) Cell coverage of the tethered *R. rubrum* cells on glass substrate in centimeter scale. Photographic (*left*) and optical microscopic (*right*) image of the DNA-Velcroed *R. rubrum* cells on the substrate after stained with Nile blue and washed. The substrate is uniformly colored blue, displaying good coverage of the cells. The inset image exhibits chemical structure of Nile blue stain. (C) Quantitative analysis of the cell coverage (# of cells/100 μm^2) in image (D-F). There are 17.3 and 0.6 cells/100 μm^2 inside and outside of the PDMS well, respectively (n = 3 and 1). The data represents mean ± standard deviation (SD). (D-F) Cell patterning of the DNA-tethered *R. rubrum* cells using a PDMS-microwell. (D) Original optical and (E, F) grey scale images of the DNA-tethered cells (E) inside and (F) outside of the PDMS well. The physical capture of DNA-tethered cells are enhanced through the well, enabling the cell patterning.

https://doi.org/10.26434/chemrxiv-2025-6pdcx **ORCID:** https://orcid.org/0000-0001-9583-9703 Content not peer-reviewed by ChemRxiv. **License:** CC BY-NC-ND 4.0

Two-dimensional MICP at a microbial monolayer

Following characterization of the DNA-immobilized cells, the *R. rubrum* were incubated with high-calcium media to promote the precipitate calcium carbonate at this interface (Figure 4A). Nutrient broth was supplemented with 0.1 M calcium acetate solution, and a homogeneous layer of calcium carbonate particles was generated at the cell-modified surface. Both bright field and phase contrast imaging of calcium carbonate particles showed good coverage of the particles on tethered cells with uniform distribution across the substrate (Figure 4B). Surprisingly, some of the generated particles were larger than the cells, reaching tens of microns in diameter (Figure 4C). The observation of particles significantly larger than the immobilized microbes clearly shows substantial production of calcium carbonate.

Just as important as the size of the particles is their morphology to support direct comparison of *R. rubrum* interfacial behavior to its suspension behavior. To observe both the microbes and the calcium carbonate particles, scanning electron microscopy (SEM) analysis with energy dispersive spectroscopy (EDS) and elemental mapping was performed using beam currents of 160 pA and 10 nA, respectively (Figure 4D). In these SEM images, it is clear that *R. rubrum* maintain their rod-like shapes and can even divide at the surface, indirectly indicating that the cells are viable following immobilization. The EDS and elemental mapping further show the co-localization of the Ca, C, O, and N on cells as well as the high concentration of calcium covering the cells for those exposed to calcium acetate. When the calcium ions or the calcium acetate solution was not present, the EDS and elemental mapping analysis of the tethered *R. rubrum* cells on glass showed no localized calcium on the cells (Figure S4). Additionally, we imaged a substrate with DNA-modified surface without cells after overnight incubation in 0.1 M calcium acetate and observed

https://doi.org/10.26434/chemrxiv-2025-6pdcx **ORCID:** https://orcid.org/0000-0001-9583-9703 Content not peer-reviewed by ChemRxiv. **License:** CC BY-NC-ND 4.0

no precipitate formation (Figure S5). These imaging results further confirm that the calcium carbonate is associated with metabolic activity of the microbes.

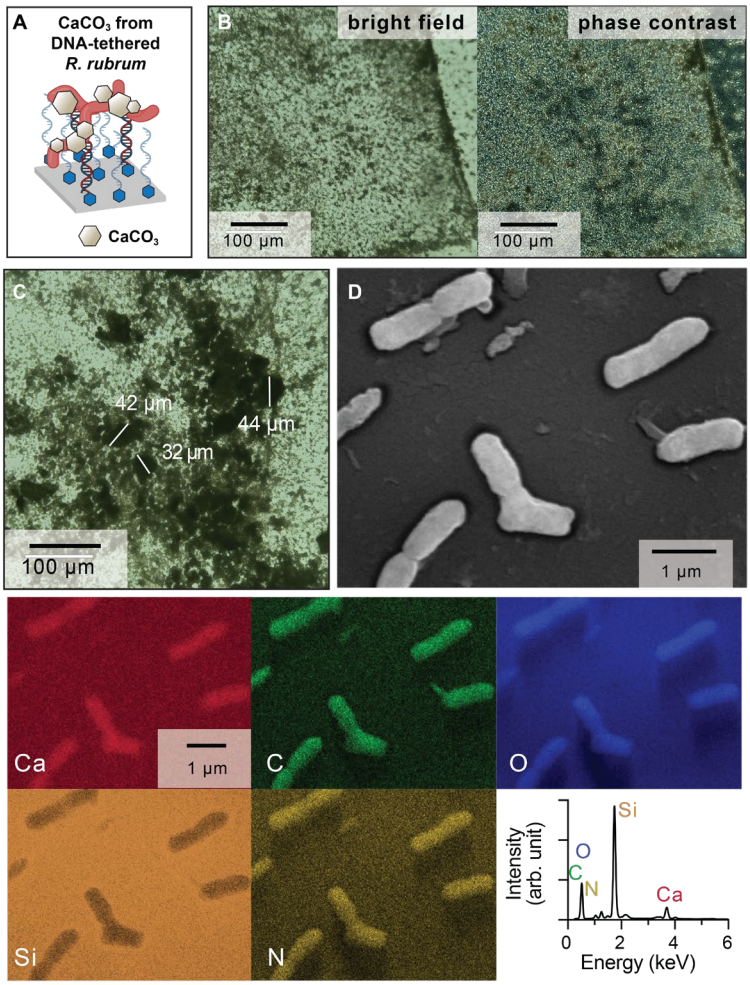


Figure 4. Microbial-induced carbonate precipitation (MICP) of *R. rubrum* on DNA-tethered surfaces. (A) Graphical illustration of DNA-tethered *R. rubrum* cells on glass substrates producing calcium carbonate precipitates the upon addition of calcium ions. (B) Optical microscopy images of the DNA-Velcroed *R. rubrum* cells with covering of calcium carbonate obtained in bright field (*left*) and phase contrast (*right*). The phase contrast image shows the calcium carbonate precipitates in better resolution. (C) Bright field image of the $CaCO_3$ particles covering the tethered cells. The particle sizes vary, and some display tens of micron in diameter. (D) SEM images of the $CaCO_3$

https://doi.org/10.26434/chemrxiv-2025-6pdcx **ORCID:** https://orcid.org/0000-0001-9583-9703 Content not peer-reviewed by ChemRxiv. **License:** CC BY-NC-ND 4.0

covered DNA-tethered *R. rubrum* cells on glass substrates. The cells conserve rod-like morphology and look healthy. Even cell division is observed on the surface. Energy dispersive spectroscopy (EDS) and elemental mapping on the SEM image shows co-localization of the Ca, C, O, and N on cells. The mapping illustrates high concentration of calcium ion on the surface of the cells. The EDS spectrum shows characteristic peaks from corresponding elements; Ca, C, O, N, and Si.

Characterization of calcium carbonate precipitates on DNA-immobilized *R. rubrum* monolayers

To further characterize the calcium precipitates on *R. rubrum* monolayers, we conducted Raman microscopy following characterization of the samples with conventional 1D Raman spectroscopy (Figure 5). The 1D Raman spectrum of the DNA-functionalized glass showed peaks corresponding to the bending vibration of the Si-O-Si bond (460-550 cm^{-1}),[43] asymmetric stretching of O-P-O in the DNA backbone (830 cm^{-1}),[44] and symmetric vibration of aromatic rings (990-1100 cm^{-1})[45] (blue line, average of n = 100). These peaks confirm DNA modification and the presence of the aromatic rings involved in the DNA conjugation reaction. After addition of the *R. rubrum*, bands associated with DNA are observable, as is a cluster of peaks in the high 1000 cm^{-1} range, which we attribute to cellular proteins[44] (brown line). The calcium carbonate particles formed by MICP in bulk solution, showed peaks consistent with the reference calcite spectrum, with expected peaks from the E_g (T), E_g (L), E_g, and A_{1g} modes, inferring the generation of calcite in solution.[46]

Following characterization by 1D Raman spectroscopy, 2D Raman was performed. As with the earlier brightfield images, optical microscopy showed homogeneous coverage of the glass with *R. rubrum* (Figure 5A,B). We additionally mapped 2D Raman spectra across this region of the glass (Figure 5C). Following exposure of the cell monolayer to calcium acetate (spot 1: red and spot 2:

https://doi.org/10.26434/chemrxiv-2025-6pdcx **ORCID:** https://orcid.org/0000-0001-9583-9703 Content not peer-reviewed by ChemRxiv. **License:** CC BY-NC-ND 4.0

orange), the surface showed bands at 584, 964, and 1091 cm^{-1}. We attribute the bands at 1091 cm^{-1} to C-O symmetric stretching mode of the calcium carbonate,[47] consistent with calcite. The bands at 584 and 964 cm^{-1} are attributed to the organic components of the cell, specifically the ring CH_2 bending and C-H bending modes, respectively.[48] As expected from the relative amounts of organic matter at the edge of the cell and middle of the cell, the 964 cm^{-1} peaks attributed to organic components are larger for the measurement in the center of the cell than those observed at the edge of the cell.

With peaks attributed to the mineral and the organic components of the system, we can take a ratio of the intensity of the Raman spectral peaks at wavelengths of 1100 and 960 cm^{-1}, or mineral to organic ratio as I_{1100}/I_{960}, providing a proxy for the relative ratio of mineral (C-O symmetric stretching of carbonate) to organic matter (C-H bending of organics) at each point in the image. The color map (Figure 5B,C) is a representation of I_{1100}/I_{960}. At the boundary of the cells, high I_{1100}/I_{960} is observed, whereas the cell interior exhibits low I_{1100}/I_{960}, indicating differences in the local concentration of calcium carbonate compared to organic matter at these two locations. When the Raman intensity map is overlaid with the optical image, localized dark spots are additionally observed, hypothesized to arise from the presence of calcium carbonate particles (Figure 5D). Despite confirming that calcium carbonate is present on the surfaces and the presence of peaks from polymorphs of calcium carbonate (calcite, vaterite, and aragonite) near 1100 cm^{-1} originating from the C-O symmetric carbonate stretching,[49] we could not conclusively determine the mineral form of the precipitated calcium carbonate. Therefore, we performed X-ray scattering characterization of calcium carbonate precipitates formed on DNA-immobilized *R. rubrum* monolayers. Although *in-house* XRD did not yield strong diffraction, owing to limited sample volume and weak X-ray interaction from the thin calcium carbonate layer, we successfully

https://doi.org/10.26434/chemrxiv-2025-6pdcx **ORCID:** https://orcid.org/0000-0001-9583-9703 Content not peer-reviewed by ChemRxiv. **License:** CC BY-NC-ND 4.0

collected distinct Bragg diffraction on a synchrotron beamline at 11-BM (CMS), National Synchrotron Light Source II (NSLS-II), Brookhaven National Laboratory using a bright and focused 13.5 keV X-ray beam (Figure 6A).

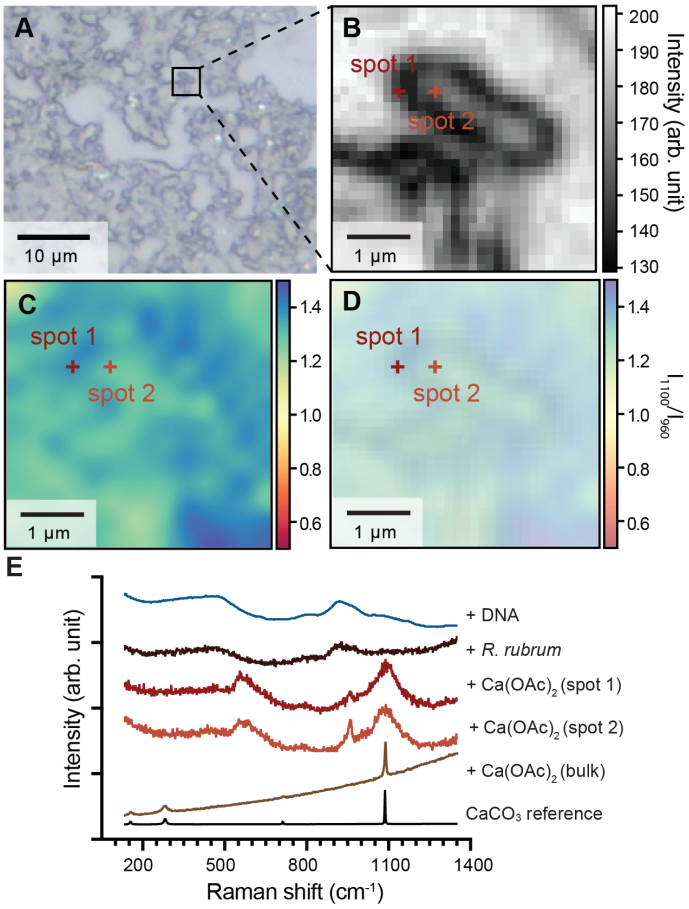


Figure 5. Characterization of $CaCO_3$ on the DNA-Velcroed *R. rubrum* via Raman spectroscopy. (A, B) Optical microscopic images of the $CaCO_3$ covered DNA-tethered *R. rubrum* cells on glass substrates in (A) zoom-out and (B) zoom-in modes. (C) 100% Raman map corresponding to the optical image (B). The intensity color map is displayed by the ratio of Raman intensity at the shifts of 1100 and 960 cm^{-1}, or I_{1100}/I_{960}. (D) 60% Raman map and 40% optical image of (B) and (C). The boundary of the cellular morphology shows high I_{1100}/I_{960} whereas the inside cell exhibits low I_{1100}/I_{960}. This spatial resolution reflects that the chemical composition at the surface of the cells is different from that inside the cells. (E) Raman spectra of the DNA-

https://doi.org/10.26434/chemrxiv-2025-6pdcx ORCID: https://orcid.org/0000-0001-9583-9703 Content not peer-reviewed by ChemRxiv. License: CC BY-NC-ND 4.0

functionalized glass substrate (blue), with DNA-Velcroed *R. rubrum* cells (brown), after addition of calcium acetate solution (spot 1 at the cell surface in red and spot 2 at the cell center in orange), calcium carbonate particle formed by MICP in bulk solution (olive), calcium carbonate reference sample (black), from *top* to *bottom*.

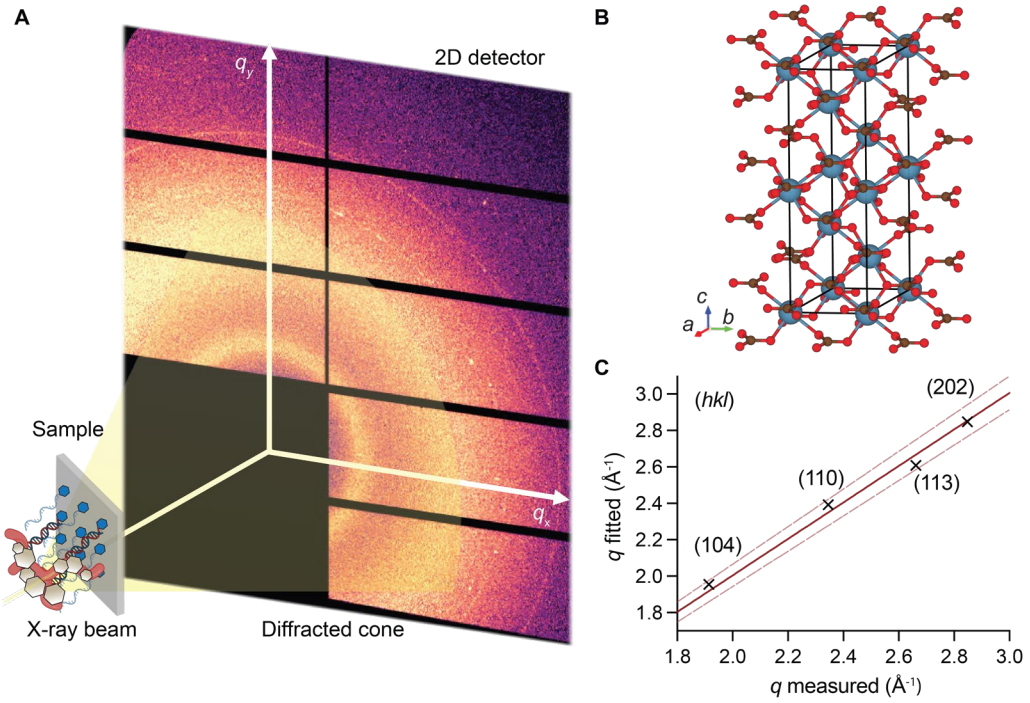


Figure 6. Characterization of crystalline $CaCO_3$ on the DNA-Velcroed *R. rubrum* via X-ray scattering. (A) Schematics of $CaCO_3$ on the DNA-Velcroed *R. rubrum* and corresponding X-ray diffraction pattern. (B) Crystal structure of calcite visualized using software VESTA.[41] The atoms are color coded; blue, brown and red are respectively calcium, carbon, and oxygen. The space group is $R\bar{3}c$ (#167-1); $a = 4.991$ Å, $\alpha = 90.0°$, $b = 4.991$ Å, $\beta = 90.0°$, $c = 17.062$ Å, $\gamma = 120.0°$.[50] (C) Parity plot of measured versus calculated Bragg peak positions (scattering vector, q) for hexagonal lattice reflections. The experimental Bragg diffraction spots were detected from the 2D image in A through fitting a bivariate normal distribution model in MATLAB-based GIXSGUI package.[51] The calculated Bragg peaks were fitted to Equation (1) across all reflections; (104),

https://doi.org/10.26434/chemrxiv-2025-6pdcx **ORCID:** https://orcid.org/0000-0001-9583-9703 Content not peer-reviewed by ChemRxiv. **License:** CC BY-NC-ND 4.0

(110), (113), (202). Data points are annotated with their corresponding (*hkl*) Miller indices. The solid line displays ideal agreement, and dotted lines show the 95% confidence interval of the lattice fit (a = 5.25 ± 0.08 Å, c = 18.16 ± 1.35 Å).

Calcite has a rhombohedral crystal structure with $R\bar{3}c$ *space group* (#167) where $a = b \neq c, \alpha = \beta = 90°, \gamma = 120°$ (Figure 6B).[50] Therefore, the lattice parameter equation shows a hexagonal setting for each (*hkl*) Miller indices, where q is scattering vector, d_{hkl} is interplanar spacing for the Miller indices (*hkl*), G is reciprocal-space metric, H is dimensionless in-plane index combination, l^2 is dimensionless squared out-of-plane index:

$$G \equiv \left(\frac{q}{2\pi}\right)^2 = \frac{1}{{d_{hkl}}^2} = \frac{4}{3}\frac{H}{a^2} + \frac{1}{c^2}l^2 \quad (1)$$

$$H \equiv h^2 + hk + k^2 \quad (2)$$

Equation (1) becomes a least-squares problem for $1/a^2$ and $1/c^2$ across all reflections.

The Bragg diffraction spots of the 2D X-ray scattering image in Figure 6A were detected by fitting a model of bivariate normal distribution on a MATLAB-based GIXSGUI package[51] (Figure S6). All the Bragg diffraction spots in scatting vectors and the corresponding (*hkl*) Miller indices are shown in Table S2. To evaluate the calcite lattice parameter model in comparison to the experimental results, we obtained a parity plot of measured versus calculated Bragg peak positions (Figure 6C). Given the assumption that our sample is calcite following our bulk analysis result in Figure 1D and the literature,[50] the Bragg diffraction peaks (104), (110), (113), (202) were fitted to give lattice constants as a = 5.25 $\pm$ 0.08 Å and c = 18.16 $\pm$ 1.35 Å (Table S3); which are comparable with the literature values as a = 4.99 Å and c = 17.06 Å.[50] Moreover, the data points annotated with their (*hkl*) indices lie within the 95% confidence interval of the lattice fit, confirming good agreement between the calcite model and the experimental data.

https://doi.org/10.26434/chemrxiv-2025-6pdcx **ORCID:** https://orcid.org/0000-0001-9583-9703 Content not peer-reviewed by ChemRxiv. **License:** CC BY-NC-ND 4.0

DISCUSSION

Despite the importance of the interface between an abiotic substrate and MICP-competent microbes, the behavior of these cells in bulk solution is often used for characterization. However, similar behavior between bulk solution and surface-associated microbes is rarely observed outside of the lab. Here, we provide a straightforward approach to generate uniform, reproducible monolayers of microbes on abiotic substrates. We demonstrate the power of this approach in a proof-of-concept system to enable the study of MICP at abiotic-biotic interfaces. Specifically, we study this process with the mixotrophic microbe *R. rubrum* under chemoheterotrophic conditions. In the bulk, *R. rubrum* generates crystalline calcite particles in solution.

To compare MICP in the bulk to that at an interface, we employ DNA hybridization-based immobilization to enable the generation of a homogeneous layer of microbes on glass substrates. Exposure of these microbial monolayers to calcium acetate provides a source of both calcium ions and a carbon source in the form of acetate. The exposure to calcium acetate results in the precipitation of calcium carbonate particles significantly larger than the immobilized cells. Although Raman could not distinguish the polymorph, synchrotron-based X-ray scattering on the DNA-immobilized *R. rubrum* single-cell monolayer resolved lattice parameters consistent with calcite. Since the morphology of the precipitate differs sufficiently from solution production, we demonstrate the importance of studying processes at interfaces as well as in bulk.

Looking forward, the integration of this 2D spatial organization into 3D consortia presents exciting opportunities for the integration of MICP-competent microbes, which can generate a protective calcium carbonate shell, mimicking the natural defenses of protection such as seashells. Such an approach could further protect synthetic biofilms or engineered microbial systems from external stresses, creating a durable and sustainable bio-hybrid material. Furthermore, the

https://doi.org/10.26434/chemrxiv-2025-6pdcx **ORCID:** https://orcid.org/0000-0001-9583-9703 Content not peer-reviewed by ChemRxiv. **License:** CC BY-NC-ND 4.0

implications of this work extend beyond biomineralization. This method can be adapted for localized production of organic bioproducts, such as functional polymers, or metallic particles that can function as catalysts. These highlight the significance of the DNA hybridization-based immobilization approach to applications in biotechnology, materials science, and environmental engineering.

In summary, this work demonstrates the importance of studying interfacial processes in biological systems in relevant environments to monitor microscopic interactions that may not be observable in the bulk. We report a universal method to enable the study of such interactions through DNA hybridization-based immobilization of cells at an abiotic surface, rapidly generating reproducible and homogeneous monolayers on substrates. As a proof-of-concept demonstration of this approach, we immobilized MICP-competent cells and demonstrate their calcium carbonate precipitation abilities and how they differ from the bulk when deployed at an interface. This DNA-based tethering approach offers a versatile platform for localizing not only cells but also the products of their metabolism such as calcium carbonate and other bioproducts, paving the way for diverse applications in biomaterials engineering, environmental remediation, and beyond.

MATERIALS AND METHODS

Microbial-induced carbonate precipitation (MICP)

For bulk-solution experiments, *R. rubrum* cells were cultured in nutrient broth (NB) medium until the culture reached an optical density at 600 nm (OD_{600}) of 1. To induce calcium carbonate precipitation, 50 mL of 0.1 M calcium acetate solution was added to 50 mL of the culture (OD_{600} = 1) in a sterile 250 mL culture flask. The mixture was incubated at 30 °C for 40 h, after which images of the precipitate were obtained.

https://doi.org/10.26434/chemrxiv-2025-6pdcx **ORCID:** https://orcid.org/0000-0001-9583-9703 Content not peer-reviewed by ChemRxiv. **License:** CC BY-NC-ND 4.0

For substrate-associated MICP, DNA-tethered *R. rubrum* cells (C2) on DNA-functionalized substrates (M2) were first prepared as described in the Supplementary Materials. DNA Sequences were as followed; 5′-/5AmMC6/ CCCTAGAGTGAGTCGTATGA-3′ (M2), 5′-/5AmMC6/ TCATACGACTCACTCTAGGG-3′ (C2) (5AmMC6 = 6-aminohexyl phosphate). M2 and C2 are ssDNA that are complementary to each other. The sandwiched cell-substrate assembly was then transferred into a 50 mL Falcon tube containing a mixture of 10 mL NB medium and 10 mL 0.1 M calcium acetate solution, providing both nutrients for microbial growth and a source of calcium ions. This setup formed microbial monolayers and subsequent calcium carbonate precipitation directly on the substrate. The Falcon tube was incubated at 30 °C for 2 – 3 days, after which visible calcium carbonate particles were observed on the substrates.

Analysis and Measurement

Optical density of cells was measured using a NanoDrop™ One Microvolume UV-Vis Spectrophotometer (Thermo Scientific, USA). X-ray diffraction (XRD) was conducted with Cu source (Kα) at 45 kV and 200 mA on Smartlab (Rigaku). The calcium carbonate sample after MICP reaction was fully dried for the XRD measurement. The cells and calcium carbonate particles were observed using a Revolve Fluorescence Microscope (Echo, USA). The scanning electron microscopy (SEM) imaging was performed on a Zeiss Merlin high-resolution scanning electron microscope (Jena, Germany) with an accelerating voltage of 3 kV. For EDS analysis, an EDS probe was inserted for the mapping with an accelerating voltage of 20 kV. The Raman microscopy was conducted on Renishaw inVia™ Reflex Micro-Raman Spectrometer (Gloucestershire, UK) using a 532 nm wavelength laser. Synchrotron X-ray scattering experiments

https://doi.org/10.26434/chemrxiv-2025-6pdcx **ORCID:** https://orcid.org/0000-0001-9583-9703 Content not peer-reviewed by ChemRxiv. **License:** CC BY-NC-ND 4.0

were conducted at beamline 11-BM (CMS), NSLS-II, Brookhaven National Laboratory, using a DECTRIS Pilatus 800K detector for the X-ray beam with an average photon energy of 13.5 keV.

Statistical analysis

Statistical analyses were performed using an unpaired t-test with Welch's correction using GraphPad Prism and Microsoft Excel. The data is expressed as the means ± standard deviation (SD).

SUPPORTING INFORMATION

The PDF file includes: Additional Materials and Methods details; Figures S1 to S6; Tables S1 to S3; References (PDF)

AUTHOR INFORMATION

Corresponding Author

*corresponding author: afurst@mit.edu

Author Contributions

The manuscript was written through contributions of all authors. All authors have given approval to the final version of the manuscript. Conceptualization: YKG, ALF Methodology: YKG, TD, MG Investigation: YKG, CCK Visualization: YKG Supervision: ALF Writing—original draft: YKG, ALF Writing—review & editing: YKG, TD, CCK, MG, ALF

https://doi.org/10.26434/chemrxiv-2025-6pdcx **ORCID:** https://orcid.org/0000-0001-9583-9703 Content not peer-reviewed by ChemRxiv. **License:** CC BY-NC-ND 4.0

Notes

The authors declare no competing financial interest. All data are available in the main text or the supporting information.

ACKNOWLEDGMENT

This research was supported by grants from a US Government Agency and the Army Research Office (W911NF2210106), an MIT Energy Initiative Seed Grant, a fellowship to MG from the Swiss National Science Foundation (SNSF) (P500PN_217800), and a grant from the MIT Chemical Engineering Comm Lab (MG). This work was performed in part through the use of MIT nano facilities. This research used beamline 11-BM (CMS) of the National Synchrotron Light Source II, a U.S. Department of Energy (DOE) Office of Science User Facility operated for the DOE Office of Science by Brookhaven National Laboratory under Contract No. DE-SC0012704.

REFERENCES

(1) Reuters. World Needs $94 Trillion Spent on Infrastructure by 2040: Report. *Reuters*. Reuters July 25, 2017. https://www.reuters.com/article/business/world-needs-94-trillion-spent-on-infrastructure-by-2040-report-idUSKBN1AA1AC/ (accessed 2025-09-17).

(2) Yang, L.; Zhang, Y.; Yan, Y. Utilization of Original Phosphogypsum as Raw Material for the Preparation of Self-Leveling Mortar. *J. Clean. Prod.* **2016**, *127*, 204–213.

(3) U.S. Geological Survey. Mineral Commodity Summaries 2020. *Mineral Commodity Summaries*. US Geological Survey: Reston, VA, 2020, p 200. https://doi.org/10.3133/mcs2020.

https://doi.org/10.26434/chemrxiv-2025-6pdcx **ORCID:** https://orcid.org/0000-0001-9583-9703 Content not peer-reviewed by ChemRxiv. **License:** CC BY-NC-ND 4.0

(4) U.S. Geological Survey. Mineral Commodity Summaries 2021. *Mineral Commodity Summaries*. US Geological Survey: Reston, VA, 2021, p 200. https://doi.org/10.3133/mcs2021.

(5) Andrew, R. M. Global CO_2 Emissions from Cement Production, 1928–2018. *Earth Syst. Sci. Data* **2019**, *11* (4), 1675–1710.

(6) World Economic Forum. Net-Zero Emissions Performance of the Cement Industry Worldwide as of 2023, 2024. https://www.statista.com/statistics/1557819/cement-industry-key-environmental-indicators/.

(7) Zhang, K.; Tang, C.-S.; Jiang, N.-J.; Pan, X.-H.; Liu, B.; Wang, Y.-J.; Shi, B. Microbial-induced Carbonate Precipitation (MICP) Technology: A Review on the Fundamentals and Engineering Applications. *Environ. Earth Sci.* **2023**, *82* (9), 229.

(8) Anbu, P.; Kang, C.-H.; Shin, Y.-J.; So, J.-S. Formations of Calcium Carbonate Minerals by Bacteria and Its Multiple Applications. *Springerplus* **2016**, *5*, 250.

(9) Bandyopadhyay, A.; Saha, A.; Ghosh, D.; Dam, B.; Samanta, A. K.; Dutta, S. Microbial Repairing of Concrete & Its Role in CO_2 Sequestration: A Critical Review. *Beni-Suef Univ. J. Basic Appl. Sci.* **2023**, *12* (1), 1–13.

(10) Wang, Y.; Konstantinou, C.; Tang, S.; Chen, H. Applications of Microbial-Induced Carbonate Precipitation: A State-of-the-Art Review. *Biogeotechnics* **2023**, *1* (1), 100008.

(11) Hemayati, M.; Nematollahi, A.; Nikooee, E.; Habibagahi, G.; Niazi, A. Non-ureolytic Microbially Induced Carbonate Precipitation: Investigating a Cleaner Biogeotechnical Engineering Pathway for Soil Mechanical Improvement. *J. Eng. (Stevenage)* **2024**, *2024* (1), e12350.

https://doi.org/10.26434/chemrxiv-2025-6pdcx **ORCID:** https://orcid.org/0000-0001-9583-9703 Content not peer-reviewed by ChemRxiv. **License:** CC BY-NC-ND 4.0

(12) Liu, J.; Li, G.; Li, X. Geotechnical Engineering Properties of Soils Solidified by Microbially Induced $CaCO_3$ Precipitation (MICP). *Adv. Civ. Eng.* **2021**, *2021*, 1–21.

(13) Prajapati, N. K.; Agnihotri, A. K.; Basak, N. Microbial Induced Calcite Precipitation (MICP) a Sustainable Technique for Stabilization of Soil: A Review. *Materials Today: Proceedings* **2023**, *93*, 357–361.

(14) Hemayati, M.; Nikooee, E.; Habibagahi, G.; Niazi, A.; Afzali, S. F. New Non-Ureolytic Heterotrophic Microbial Induced Carbonate Precipitation for Suppression of Sand Dune Wind Erosion. *Sci. Rep.* **2023**, *13* (1), 5845.

(15) Murugan, R.; Suraishkumar, G. K.; Mukherjee, A.; Dhami, N. K. Influence of Native Ureolytic Microbial Community on Biocementation Potential of Sporosarcina Pasteurii. *Sci. Rep.* **2021**, *11* (1), 20856.

(16) Bai, H.; Liu, D.; Zheng, W.; Ma, L.; Yang, S.; Cao, J.; Lu, X.; Wang, H.; Mehta, N. Microbially-Induced Calcium Carbonate Precipitation by a Halophilic Ureolytic Bacterium and Its Potential for Remediation of Heavy Metal-Contaminated Saline Environments. *Int. Biodeterior. Biodegradation* **2021**, *165*, 105311.

(17) Fang, C.; Achal, V. Enhancing Carbon Neutrality: A Perspective on the Role of Microbially Induced Carbonate Precipitation (MICP). *Biogeotechnics* **2024**, *2* (2), 100083.

(18) Zhu, T.; Dittrich, M. Carbonate Precipitation through Microbial Activities in Natural Environment, and Their Potential in Biotechnology: A Review. *Front. Bioeng. Biotechnol.* **2016**, *4*, 4.

https://doi.org/10.26434/chemrxiv-2025-6pdcx **ORCID:** https://orcid.org/0000-0001-9583-9703 Content not peer-reviewed by ChemRxiv. **License:** CC BY-NC-ND 4.0

(19) Smith, C.; Hill, A. K.; Torrente-Murciano, L. Current and Future Role of Haber–Bosch Ammonia in a Carbon-Free Energy Landscape. *Energy Environ. Sci.* **2020**, *13* (2), 331–344.

(20) Zhu, T.; Merroun, M. L.; Arhonditsis, G.; Dittrich, M. Attachment on Mortar Surfaces by Cyanobacterium Gloeocapsa PCC 73106 and Sequestration of CO_2 by Microbially Induced Calcium Carbonate. *Microbiologyopen* **2021**, *10* (5), e1243.

(21) Benzerara, K.; Skouri-Panet, F.; Li, J.; Férard, C.; Gugger, M.; Laurent, T.; Couradeau, E.; Ragon, M.; Cosmidis, J.; Menguy, N.; Margaret-Oliver, I.; Tavera, R.; López-García, P.; Moreira, D. Intracellular Ca-Carbonate Biomineralization Is Widespread in Cyanobacteria. *Proc. Natl. Acad. Sci. U. S. A.* **2014**, *111* (30), 10933–10938.

(22) Konstantinou, C.; Wang, Y. Unlocking the Potential of Microbially Induced Calcium Carbonate Precipitation (MICP) for Hydrological Applications: A Review of Opportunities, Challenges, and Environmental Considerations. *Hydrology* **2023**, *10* (9), 178.

(23) Almajed, A.; Lateef, M. A.; Moghal, A. A. B.; Lemboye, K. State-of-the-Art Review of the Applicability and Challenges of Microbial-Induced Calcite Precipitation (MICP) and Enzyme-Induced Calcite Precipitation (EICP) Techniques for Geotechnical and Geoenvironmental Applications. *Crystals (Basel)* **2021**, *11* (4), 370.

(24) Fan, G.; Corbin, N.; Chung, M.; Gill, T. M.; Moore, E. B.; Karbelkar, A. A.; Furst, A. L. Highly Efficient Carbon Dioxide Electroreduction via DNA-Directed Catalyst Immobilization. *JACS Au* **2024**, *4* (4), 1413–1421.

(25) Furst, A. L.; Smith, M. J.; Francis, M. B. Direct Electrochemical Bioconjugation on Metal Surfaces. *J. Am. Chem. Soc.* **2017**, *139* (36), 12610–12616.

https://doi.org/10.26434/chemrxiv-2025-6pdcx **ORCID:** https://orcid.org/0000-0001-9583-9703 Content not peer-reviewed by ChemRxiv. **License:** CC BY-NC-ND 4.0

(26) Furst, A. L.; Klass, S. H.; Francis, M. B. DNA Hybridization to Control Cellular Interactions. *Trends Biochem. Sci.* **2019**, *44* (4), 342–350.

(27) Furst, A. L.; Smith, M. J.; Lee, M. C.; Francis, M. B. DNA Hybridization to Interface Current-Producing Cells with Electrode Surfaces. *ACS Cent. Sci.* **2018**, *4* (7), 880–884.

(28) Twite, A. A.; Hsiao, S. C.; Onoe, H.; Mathies, R. A.; Francis, M. B. Direct Attachment of Microbial Organisms to Material Surfaces through Sequence-Specific DNA Hybridization. *Adv. Mater.* **2012**, *24* (18), 2380–2385.

(29) Palla, K. S.; Hurlburt, T. J.; Buyanin, A. M.; Somorjai, G. A.; Francis, M. B. Site-Selective Oxidative Coupling Reactions for the Attachment of Enzymes to Glass Surfaces through DNA-Directed Immobilization. *J. Am. Chem. Soc.* **2017**, *139* (5), 1967–1974.

(30) Mongili, B.; Fino, D. Carbon Monoxide Fermentation to Bioplastic: The Effect of Substrate Adaptation on Rhodospirillum Rubrum. *Biomass Conversion and Biorefinery* **2021**, *11* (2), 705–714.

(31) Eisenberg, M. A. The Tricarboxylic Acid in Rhodospirillum Rubrum. *J. Biol. Chem.* **1953**, *203* (2), 815–836.

(32) Anderson, L.; Fuller, R. C. Photosynthesis in Rhodospirillum Rubrum. I. Autotrophic Carbon Dioxide Fixation. *Plant Physiol.* **1967**, *42* (4), 487–490.

(33) Tabita, F. R. The Biochemistry and Metabolic Regulation of Carbon Metabolism and CO_2 Fixation in Purple Bacteria. In *Advances in Photosynthesis and Respiration*; Kluwer Academic Publishers: Dordrecht, 2006; pp 885–914.

https://doi.org/10.26434/chemrxiv-2025-6pdcx **ORCID:** https://orcid.org/0000-0001-9583-9703 Content not peer-reviewed by ChemRxiv. **License:** CC BY-NC-ND 4.0

(34) Wang, D.; Zhang, Y.; Pohlmann, E. L.; Li, J.; Roberts, G. P. The Poor Growth of Rhodospirillum Rubrum Mutants Lacking RubisCO Is Due to the Accumulation of Ribulose-1,5-Bisphosphate. *J. Bacteriol.* **2011**, *193* (13), 3293–3303.

(35) Gill, S. R.; Fedorka-Cray, P. J.; Tweten, R. K.; Sleeper, B. P. Purification and Properties of the Carbonic Anhydrase of Rhodospirillum Rubrum. *Arch. Microbiol.* **1984**, *138* (2), 113–118.

(36) Sarkar, A.; Mahapatra, S. Synthesis of All Crystalline Phases of Anhydrous Calcium Carbonate. *Cryst. Growth Des.* **2010**, *10* (5), 2129–2135.

(37) de Leeuw, N. H.; Parker, S. C. Surface Structure and Morphology of Calcium Carbonate Polymorphs Calcite, Aragonite, and Vaterite: An Atomistic Approach. *J. Phys. Chem. B* **1998**, *102* (16), 2914–2922.

(38) Wyckoff, R. W. G. The Crystal Structures of Some Carbonates of the Calcite Group. *Am. J. Sci.* **1920**, *s4-50* (299), 317–360.

(39) De Villiers, J. P. R. Crystal Structures of Aragonite, Strontianite, and Witherite. *Am. Mineral.* **1971**, *56* (5–6), 758–767.

(40) Wang, J.; Becker, U. Structure and Carbonate Orientation of Vaterite ($CaCO_3$). *Am. Mineral.* **2009**, *94* (2–3), 380–386.

(41) Momma, K.; Izumi, F. VESTA 3 for Three-Dimensional Visualization of Crystal, Volumetric and Morphology Data. *J. Appl. Crystallogr.* **2011**, *44* (6), 1272–1276.

(42) Schindelin, J.; Arganda-Carreras, I.; Frise, E.; Kaynig, V.; Longair, M.; Pietzsch, T.; Preibisch, S.; Rueden, C.; Saalfeld, S.; Schmid, B.; Tinevez, J.-Y.; White, D. J.; Hartenstein, V.;

https://doi.org/10.26434/chemrxiv-2025-6pdcx **ORCID:** https://orcid.org/0000-0001-9583-9703 Content not peer-reviewed by ChemRxiv. **License:** CC BY-NC-ND 4.0

Eliceiri, K.; Tomancak, P.; Cardona, A. Fiji: An Open-Source Platform for Biological-Image Analysis. *Nat. Methods* **2012**, *9* (7), 676–682.

(43) Ben Khemis, S.; Burov, E.; Montigaud, H.; Skrelic, D.; Gouillart, E.; Cormier, L. Structural Analysis of Sputtered Amorphous Silica Thin Films: A Raman Spectroscopy Investigation. *Thin Solid Films* **2021**, *733* (138811), 138811.

(44) Kuhar, N.; Sil, S.; Verma, T.; Umapathy, S. Challenges in Application of Raman Spectroscopy to Biology and Materials. *RSC Adv.* **2018**, *8* (46), 25888–25908.

(45) Edwards, H. G. M. Spectra-Structure Correlations in Raman Spectroscopy. *Handbook of Vibrational Spectroscopy*; Chalmers, J. M., Ed.; John Wiley & Sons, Ltd: Chichester, UK, 2006. https://doi.org/10.1002/0470027320.s4103.

(46) Dufresne, W. J. B.; Rufledt, C. J.; Marshall, C. P. Raman Spectroscopy of the Eight Natural Carbonate Minerals of Calcite Structure. *J. Raman Spectrosc.* **2018**, *49* (12), 1999–2007.

(47) Ma, Y.; Yan, W.; Sun, Q.; Liu, X. Raman and Infrared Spectroscopic Quantification of the Carbonate Concentration in K_2CO_3 Aqueous Solutions with Water as an Internal Standard. *Geosci. Front.* **2021**, *12* (2), 1018–1030.

(48) Pezzotti, G. Raman Spectroscopy in Cell Biology and Microbiology. *J. Raman Spectrosc.* **2021**, *52* (12), 2348–2443.

(49) Dickinson, S. R.; McGrath, K. M. Quantitative Determination of Binary and Tertiary Calcium Carbonate Mixtures Using Powder X-Ray Diffraction. *Analyst* **2001**, *126* (7), 1118–1121.

(50) Maslen, E. N.; Streltsov, V. A.; Streltsova, N. R. X-Ray Study of the Electron Density in Calcite, $CaCO_3$. *Acta Crystallogr. B* **1993**, *49* (4), 636–641.

https://doi.org/10.26434/chemrxiv-2025-6pdcx **ORCID:** https://orcid.org/0000-0001-9583-9703 Content not peer-reviewed by ChemRxiv. **License:** CC BY-NC-ND 4.0

(51) Jiang, Z. *GIXSGUI*: A MATLAB Toolbox for Grazing-Incidence X-Ray Scattering Data Visualization and Reduction, and Indexing of Buried Three-Dimensional Periodic Nanostructured Films. *J. Appl. Crystallogr.* **2015**, *48* (3), 917–926.

https://doi.org/10.26434/chemrxiv-2025-6pdcx **ORCID:** https://orcid.org/0000-0001-9583-9703 Content not peer-reviewed by ChemRxiv. **License:** CC BY-NC-ND 4.0